Agricultural Water Management 291 (2024) 108616

Contents lists available at ScienceDirect

Agricultural Water Management

journal homepage: www.elsevier.com/locate/agwat

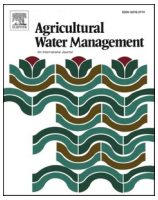

A robust model for diagnosing water stress of winter wheat by combining UAV multispectral and thermal remote sensing

Jingjing Wang [a], Yu Lou [b], Wentao Wang [a], Suyi Liu [a], Haohui Zhang [a], Xin Hui [a], Yunling Wang [a], Haijun Yan [a,d,*], Wouter H. Maes [c,**]

[a] College of Water Resources and Civil Engineering, China Agricultural University, Beijing 100083, China
[b] Science and Technology Promotion Center, Ministry of Water Resources, Beijing 100038, China
[c] UAV Research Centre, Department of Plants and Crops, Ghent University, Ghent 9000, Belgium
[d] Engineering Research Center for Agricultural Water-Saving and Water Resources, Ministry of Education, Beijing 100083, China

ARTICLE INFO

Handling Editor - B.E. Clothier

Keywords:
Multispectral
Thermal
Normalized stomatal conductance
Effective water content
Machine learning
Robustness

ABSTRACT

Diagnosing water conditions timely and accurately is crucial for seasonal irrigation scheduling in crop production. The purpose of this study was to establish robust water deficit models of winter wheat in different growing seasons by combining unmanned aerial vehicle (UAV) multispectral and thermal images. In 2021 and 2022, a water deficit field experiment on winter wheat was carried out in Hebei Province, China. Five-band multispectral and thermal images were obtained with a UAV at six key growth stages of winter wheat. Fourteen vegetation indices (VIs) and two thermal indices (TIs) were calculated. Simultaneously, wheat stomatal conductance and soil water content were measured. On this basis, normalized stomatal conductance (NGS) and effective water content (EWC) were calculated. TIs had the highest correlation with NGS and EWC at early growth stages, whereas ratio vegetation index (RVI), modified simple ratio index (MSR) and normalized difference vegetation index (NDVI) were highly correlated at later stages. Partial least squares (PLS), support vector machine (SVM) and gradient boosting decision tree (GBDT) were used to predict NGS and EWC for each growth stage, with the data of 2021 as the training set and the data of 2022 as independent test set. In general, GBDT outperformed PLS and SVM, and NGS was better predicted than EWC. Including VIs and TIs effectively improved the estimation accuracy of the predictive models. The test set results of the NGS and EWC models built by GBDT achieved the best performance in flowering stage (coefficient of determination (R^2) = 0.88, root mean square error (RMSE) = 0.08, normalized root mean square error (NRMSE) = 14.7%) and filling stage (R^2 = 0.90, RMSE = 0.05, NRMSE = 15.9%), respectively. The models of the post-heading stage were better than those of the pre-heading stage for both NGS and EWC. This study provides a robust method for diagnosing water stress only using UAV remote sensing data.

1. Introduction

Wheat is the food crop with the largest planting area and the widest distribution in the world (Reynolds and Braun, 2022). Irrigation is vital for agricultural production as irrigated wheat yield increases by about 34 % compared with rainfed yield on a global scale (Wang et al., 2021). However, irrigated agriculture accounts for about 70% of the freshwater withdrawals in the world (FAO, 2023), putting pressure on the global water cycle. Precision irrigation enables quantitative decision-making and variable inputs of irrigation amount by considering spatial and temporal variations in crop water demand (Abioye et al., 2020; Daccache et al., 2015). Thus, water use can be managed more efficiently through precision irrigation management. This requires accurate information on the spatial variation of plant and soil water status and water requirement (Maes and Steppe, 2019), which can enable the formulation of plans for variable irrigation in large-scale production.

Water stress reduces the transpiration and stomatal conductance, resulting in an increase in canopy temperature (Jackson et al., 1981; Kögler and Söffker, 2019; Buckley, 2019). This change can be observed reliably with thermal remote sensing, although corrections for weather

* Corresponding author at: College of Water Resources and Civil Engineering, China Agricultural University, Beijing 100083, China.
** Corresponding author.
E-mail addresses: yanhj@cau.edu.cn (H. Yan), wouter.maes@ugent.be (W.H. Maes).

https://doi.org/10.1016/j.agwat.2023.108616
Received 6 June 2023; Received in revised form 27 November 2023; Accepted 1 December 2023
Available online 8 December 2023

conditions and vegetation characteristics are needed to interpret the signal (Maes and Steppe, 2012; Maes et al., 2016). Measurements of canopy reflectance in the visual and near infrared are also commonly implemented for diagnosing crop water stress (Das et al., 2022; Traore et al., 2021; Zhou et al., 2021), but provide information only in an advanced stage of water stress, when the canopy structure (e.g., leaf angle distribution, reductions in leaf area) or leaf characteristics (e.g., reduction in chlorophyll, increase in photoprotective pigments as carotenes or anthocyanins) are affected (Han et al., 2020). Yang et al. (2020) pointed out that normalized difference red-edge index (NDRE) and red-edge chlorophyll index (RECI) can detect the water status of wheat under water stress and can be used to monitor crop efficiency under varying water dosages. Bhandari et al. (2021) found that excess green index (ExG), normalized difference vegetation index (NDVI) and NDRE were positively correlated with wheat yield at flowering stage and filling stage under water stress condition compared to that at early growth stages.

Satellite remote sensing can be used to monitor crop water conditions on a large scale (Bhattarai et al., 2017; Veysi et al., 2017). However, thermal data are not yet available at high spatial and spectral resolution, and multispectral reflectance data can be affected by clouds and offers limited spatial and temporal resolutions (Ezenne et al., 2019). Remote sensing with unmanned aerial vehicles (UAVs) provides the advantages of wide coverage, short measurement cycles, low cost, and flexible operation (Feng et al., 2021; Gago et al., 2015; Maes and Steppe, 2019). Applying UAVs also permits simultaneous measurements with multiple sensors (Maes and Steppe, 2019). Combining data from different sensors taps into different sources of information (Zhang et al., 2015) and can be useful in water stress research, particularly when focusing on water stress modelling. Moran et al. (1994) calculated the water deficit index (WDI) that combined thermal, multispectral, and meteorological data, which provided accurate estimation of alfalfa field evapotranspiration rates and relative field water deficit. Abuzar et al. (2009) built a modified trapezoid water stress model by combining UAV thermal and multispectral images that can be used both in wheat irrigated and rainfed situations. Cheng et al. (2022) showed that a soil water content model of corn that combined RGB, multispectral and thermal data resulted in higher accuracies than the single variable model. However, analyzing data obtained from different sensors is challenging. Few studies have used a combination of multispectral and thermal data from UAV platforms to assess stomatal conductance and soil water content in winter wheat. Another limitation of most previous studies is that the training and test datasets are not independent, resulting in an overly optimistic appraisal of the model performance. Therefore, it is necessary to investigate whether UAV remote sensing can improve the applicability of water stress models for different wheat growing seasons and stages, with separate training and test datasets.

The goal of this study was to develop an accurate, comprehensive yet robust model to estimate water deficit (using normalized stomatal conductance and effective water content) at the different growth stages of winter wheat, based solely on UAV data. To ensure that the resulting models were more robust, they were trained and tested on datasets acquired in different years. We investigated whether a combination of multispectral and thermal imagery improves the model robustness compared to multispectral data alone. For this purpose, we evaluated the performance of different machine learning methods (partial least squares (PLS), support vector machine (SVM) and gradient boosting decision tree (GBDT)).

2. Materials and methods

2.1. Study area and experimental treatments

The experiment was conducted at the China Agricultural University Experimental Station in Zhuozhou (39.45°N, 115.85°E), Hebei Province, China. The study area climate is warm summer continental (Dwb under the Köppen classification) with a summer precipitation pattern. The annual precipitation is about 560 mm, and the annual mean temperature is about 11.6 ℃.

The soil is mainly sandy (using the definition of the soil texture triangle recommended by the USDA) (Shirazi and Boersma, 1984). The average field capacity (FC) and the wilting point (WP) in the 0–40 cm soil layer are 0.24 cm^3 cm^{-3} and 0.05 cm^3 cm^{-3}, respectively. Before sowing, the soil was sampled to test physicochemical properties. The content of soil organic carbon, available phosphorus, nitrate nitrogen, and ammonia nitrogen were 20.2 g kg^{-1}, 32.5 mg kg^{-1}, 14.0 mg kg^{-1}, and 4.6 mg kg^{-1}, respectively, acquired with ultraviolet-visible spectrophotometer. The content of exchangeable potassium was 55.0 mg kg^{-1}, obtained by atomic absorption spectroscopy. Table 1 shows the sowing parameters of winter wheat. In the second year, the wheat grains harvested in the first year were used as seeds. To ensure a sufficient number of initial seedlings, the sowing rate in 2022 exceeded that of 2021 by an additional 60 kg ha^{-1}.

To collect and diagnose the water deficit in winter wheat, an experiment was carried out from March to June in 2021 and 2022. The field was divided into 12 experimental zones, corresponding to 4 irrigation levels, namely HD (high deficit), MD (moderate deficit), SD (slight deficit), and LI (local irrigation). We chose the LI as a control irrigation level to find the differences among treatments resulting from irrigation levels based on local irrigation management. In the present study, the main root depth was within a range of 40 cm. Therefore, when the average soil water content (SWC) in 0–40 cm soil layer of LI treatment dropped to around 65% FC, all zones were irrigated. The irrigation amount of LI treatment was equivalent to the average water depth that could supplement current SWC to 100% FC. In total, the irrigation amount of LI treatment in 2021 and 2022 were 270 mm and 235 mm respectively, which included 30 mm of overwintering water on November 16, 2020 and November 27, 2021. The irrigation rates for HD, MD, and SD treatments were set at 55%, 70%, and 85% of the irrigation rate applied in the LI treatment, respectively. In each experimental zone, 3 sampling plots of 6 m × 6 m were selected, resulting in a total of 36 plots. The specific experimental layout is shown in Fig. 1. Fig. 2 shows the irrigation amount of the 4 treatments as well as the cumulative reference crop evapotranspiration (ET_0, Penman-Monteith) and rainfall in the experiment.

To achieve variable rate irrigation, the experimental field was irrigated by a three-span center-pivot irrigation system with a radius of 140 m, which was equipped with solenoid valves, valve controllers, Beidou RTK receivers, and control software. The Beidou RTK receiver determined the position of the center pivot in the field for the real time identification of control zones. There were a total of 34 low-pressure sprinklers, and each sprinkler could be operated separately by turning the solenoid on or off. The designed application depths in specific control zones were obtained by changing the travel speed of the center pivot and the duty cycle of each solenoid valve (Hui et al., 2022) (Fig. 1).

2.2. UAV image acquisition

2.2.1. UAV remote sensing platform

A DJI M300 Pro UAV (Shenzhen DJI Sciences and Technologies Ltd,

Table 1
Sowing parameters of winter wheat.

	2021	2022
Cultivar	Nongda 212	Nongda 212
Sowing time	12/10/2020	10/10/2021
Seed rate (kg ha^{-1})	270	330
Row spacing (cm)	15	15
Nitrogen fertilizer amount (kg ha^{-1})	254	254
Phosphorus fertilizer amount (kg ha^{-1})	138	138
Potassium fertilizer amount (kg ha^{-1})	81	81
Organic fertilizer amount (kg ha^{-1})	22,500	-

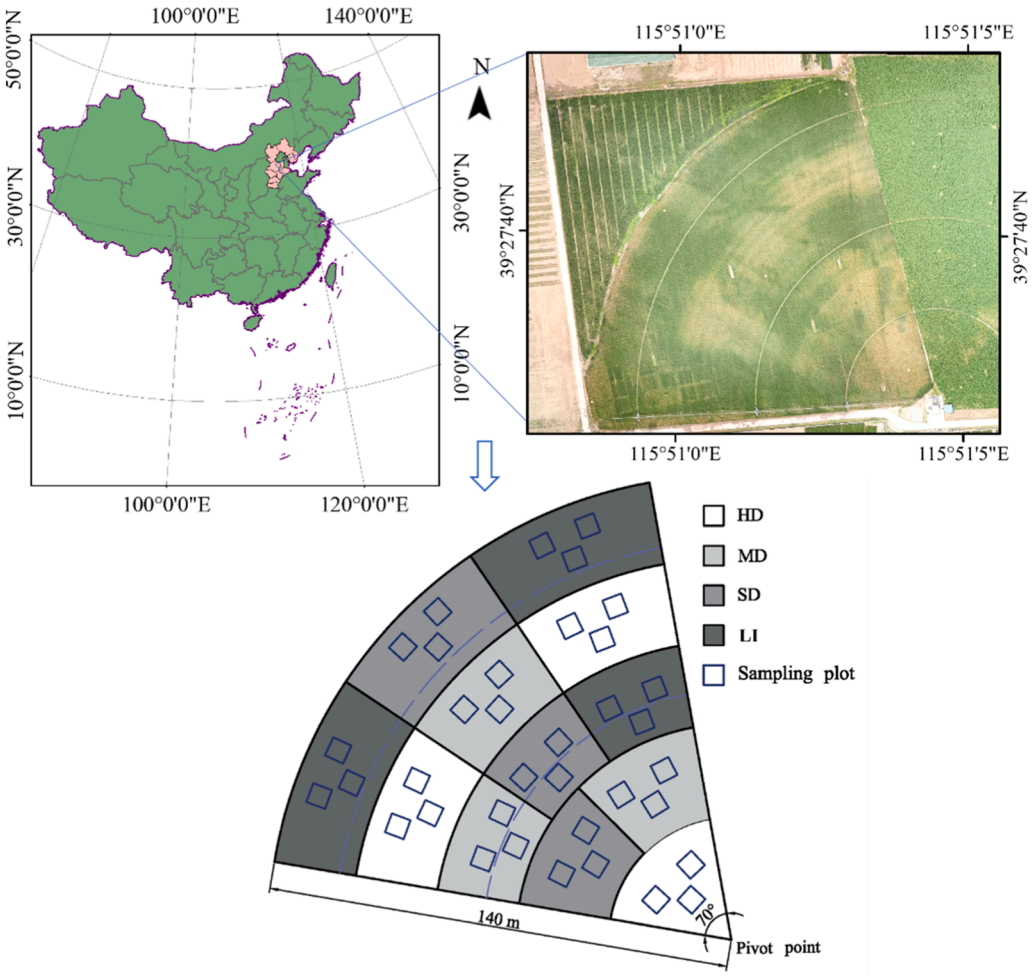

Fig. 1. Location and treatments of the experiment in this study. HD, MD, SD and LI represent high deficit, moderate deficit, slight deficit and local irrigation, respectively.

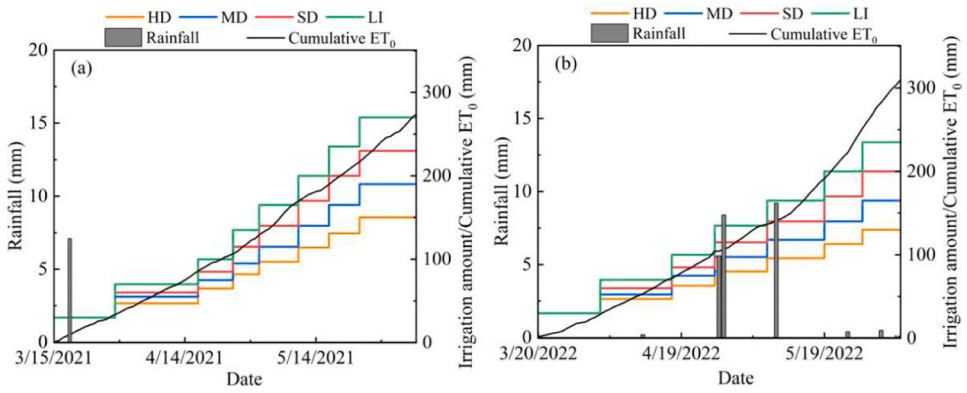

Fig. 2. Irrigation amounts of four irrigation treatments, cumulative ET_0 and rainfall in 2021 and 2022. HD, MD, SD and LI represent high deficit, moderate deficit, slight deficit and local irrigation, respectively. ET_0 represents reference crop evapotranspiration. The overwintering water amount of 30 mm was applied on November 16, 2020 and November 27, 2021, respectively.

Shenzhen, China) (maximum take-off weight of 9 kg, maximum payload 2.7 kg, maximum flight time of 55 min without payload) was equipped with a 5-band multispectral camera (MicaSense Red Edge-MX multispectral camera, AgEagle, Wichita, KS, USA) and a thermal infrared camera (DJI Zenmuse H20T). Flights were performed in clear sky and low wind speed conditions, between 11:00 and 13:00 local time. The DJI Pilot app was used for all flights planning, set at 75% forward and 75% side overlap in image acquisition for the thermal imagery. The flight height was 50 m and the flight speed was 2.1 m s^{-1}. The flight time and flight conditions (see Section 2.3.3 for a description of the weather station) are listed in Table 2.

Five ground control points (GCPs) were placed in the experimental area, and their exact location was retrieved with an RTK GNSS receiver (M600 mini, Compass Navigation, China). The adopted positioning

Table 2
The flight time of the UAV and the corresponding meteorological parameters.

Growth stages	2021						2022					
	Date	Time	$T_a^{[a]}$ (℃)	RH (%)	RS (W m^{-2})	WS (m s^{-1})	Date	Time	T_a (℃)	RH (%)	RS (W m^{-2})	WS (m s^{-1})
Tillering(T1)	06/04/2021	12:05–12:30	19.8	42.8	391.9	0.8	08/04/2022	11:30–11:55	19.5	54.6	668.1	0.5
Jointing (T2)	22/04/2021	12:25–12:50	16.1	72.1	686.9	1.2	15/04/2022	12:45–13:00	19.4	27.1	788.1	1.2
Booting(T3)	30/04/2021	12:45–13:10	14.8	54.2	610.6	1.8	25/04/2022	13:00–13:25	26.0	65.7	649.4	0.3
Heading(T4)	07/05/2021	12:10–12:35	25.7	24.1	818.1	1.0	04/05/2022	12:25–12:50	31.4	38.1	814.4	0.8
Flowering(T5)	11/05/2021	12:35–13:00	25.6	52.3	751.9	1.3	11/05/2022	11:45–12:10	19.5	49.6	538.5	1.4
Filling(T6)	27/05/2022	12:10–12:35	28.6	27.9	906.9	1.5	26/05/2022	11:45–12:10	32.6	13.5	800.4	1.5

Note: $^{[a]}T_a$, air temperature (℃); RH, relative humidity (%); RS, solar radiation (W m^{-2}); WS, wind speed (m s^{-1}).

protocol was Qianxun Find CM (Qianxun SI, China) with a horizontal accuracy of 2 cm and an elevation accuracy of 5 cm.

2.2.2. Multispectral camera

The RedEdge-MX multispectral camera is a global shutter sensor with 5 spectral bands, namely in the blue (465–485 nm), green (550–570 nm), red (663–673 nm), red edge (712–722 nm), and near-infrared (820–860 nm) spectrum. The focal length is 5.5 mm, resulting in a field of view of 47.2° and ground sampling distance of 3.5 cm at 50 m flight height. During the flights, the camera was connected to the DLS-2 sensor, measuring GNSS position and downwelling light. The camera was set up to capture an image every 2 s. A standard grey panel (Calibrated Reflectance Panel (CRP), MicaSense) was photographed for radiometric correction before each flight.

2.2.3. Thermal camera

Simultaneously, the Zenmuse H20T collected thermal images. It is an integrated camera that contains 4 sensors for a radiometric thermal camera, a wide angle camera, a zoom camera and a laser rangefinder. The thermal imaging camera is a radiometric microbolometer camera with a single band sensitivity in the 8–14 μm spectral range, a temperature range of −40 to 150 °C, and a resolution of 640 × 512 pixels. Its lens has a focal length of 13.5 mm, resulting in a field of view of 40.6° and a ground sampling distance of 4.5 cm at 50 m flight height. Images were acquired every 2 s.

The at-sensor radiance was converted into brightness temperature (T_{br}, K) using the DJI Thermal SDK 1.2 software to perform the atmospheric correction, with the locally measured air temperature (T_a), relative humidity, and flight height. The surface temperature (T_s, K) was then calculated as Eq. 1 (Maes et al., 2017; Maes and Steppe, 2012):

$$T_s = \sqrt[4]{\frac{T_{br}^4 - (1-\varepsilon) \times T_{bg}^4}{\varepsilon}} \quad (1)$$

$$T_{bg} = \sqrt[4]{0.7 \times T_a^4} \quad (2)$$

In which ε is the emissivity, estimated as 0.99. T_{bg} is the background temperature (K), calculated from air temperature (K) as Eq. 2.

2.2.4. Data processing

Pix4D Mapper (Pix4D 4.4, Pix4D S.A., Switzerland) was used to create orthomosaics with the coordinates of five GCPs as input for georeferencing. For the multispectral data, the software also converted the data to reflectance using the DLS2 and the grey reference panel measurement, which is a relatively reliable way for processing these data (Daniels et al., 2023).

The multispectral and thermal orthomosaics were imported into QGIS 3.22 (QGIS Geographic Information System; Open Source Geospatial Foundation Project), which was used for all further GIS processing. Fourteen vegetation indices that are commonly used for crop growth monitoring were calculated from the multispectral orthomosaic (Table 3). From the thermal data, two thermal indices (TIs), including

Table 3
Equations for vegetation indices.

Vegetation Indices	Formula	References
Ratio vegetation index, RVI	$RVI = NIR/R^{[a]}$	(Jordan et al., 1969)
Normalized difference vegetation index, NDVI	$NDVI = (NIR - R)/(NIR + R)$	(Rouse et al., 1974)
Normalized difference red-edge, NDRE	$NDRE = (NIR - RE)/(NIR + RE)$	(Fitzgerald et al., 2010)
Enhanced vegetation index, EVI	$EVI = 2.5 \times (NIR - R)/(NIR + 6R - 7.5B + 1)$	(Liu and Huete, 2019)
Optimized soil adjusted vegetation index, OSAVI	$OSAVI = 1.16 \times (NIR - R)/(NIR + R + 0.16)$	(Rondeaux et al., 1996)
Difference vegetation index, DVI	$DVI = NIR - R$	(Broge and Mortensen, 2002)
Green normalized difference vegetation index, GNDVI	$GNDVI = (NIR - G)/(NIR + G)$	(Gitelson et al., 1995)
Red-edge chlorophyll index, CIRE	$CIRE = NIR/RE - 1$	(Gitelson et al., 2005)
Enhanced vegetation index, EVI2	$EVI2 = 2.5 \times (NIR - R)/(NIR + 2.4R + 1)$	(Jiang et al., 2008)
Green optimal soil adjusted vegetation index, GOSAVI	$GOSAVI = 1.16 \times (NIR - G)/(NIR + G + 0.16)$	(Cao et al., 2015)
Modified simple ratio index, MSR	$MSR = (NIR/R - 1)/\left[(NIR/R)^{0.5} + 1\right]$	(Haboudane et al., 2004)
Soil adjusted vegetation index, SAVI	$SAVI = 1.5 \times (NIR - R)/(NIR + R + 0.5)$	(Huete, 1988)
Structure insensitive pigment index, SIPI	$SIPI = (NIR - B)/(NIR - R)$	(Penuelas et al., 1995)
Red-edge vegetation index, RERVI	$RERVI = NIR/RE$	(Cao et al., 2013)

Note: $^{[a]}$NIR, RE, R, G and B are reflectance values of wheat in near-infrared, red-edge, red, green, and blue band from multispectral camera.

the difference between canopy temperature and air temperature (△T, ℃) and crop water stress index (CWSI) were calculated as follows (Eqs. 3 and 4):

$$\Delta T = T_s - T_a \quad (3)$$

$$CWSI = \frac{T_s - T_{pot}}{T_{dry} - T_{pot}} \quad (4)$$

With T_{pot} (℃) and T_{dry} (℃) corresponding to the surface temperature of a winter wheat plant transpiring at a maximal rate (T_{pot}) and not transpiring at all (T_{dry}). In this case, T_{pot} and T_{dry} were calculated directly per measurement day using the histogram method, as the 1st and 99th percentile the polygon records of that day (De Swaef et al., 2021). The histogram method can be applied in this case, since the different irrigation treatments guarantee that at least some completely unstressed and some severely stressed plants are present on each measurement day.

The normalized difference vegetation index (NDVI) images were converted to binary images by the vegetation index threshold (OTSU) (Otsu, 1979) to distinguish vegetation from soil background. Then, the average value for each VI and TI of each sample plot was extracted using

the zonal statistics function.

2.3. Field data acquisition

2.3.1. Stomatal conductance

A leaf porometer (SC-1, METER, USA) was used to measure the stomatal conductance (GS) of three wheat flag leaves per plot from 11:00–13:00 on the same day of the UAV flight. As recommended, the probe was regularly calibrated, and the sensor probe was kept horizontally during all measurements.

2.3.2. Soil water content

A TDR device (Trime-T3, IMKO Ltd., Ettlingen, Germany) was used to monitor the soil water content (SWC) at depths of 0–20 cm and 20–40 cm. 36 Trime tubes were buried at the center of each plot. The soil was extracted with a soil drill next to the trime tube to calibrate the TDR measurements.

2.3.3. Meteorological parameters

During the remote sensing image acquisition, a hand-held meteorograph (4500 DT, Kestrel, USA) was used to measure the instantaneous meteorological data, including relative humidity, temperature, and wind speeds at 2 m height. Additionally, a weather station (HOBO U30, Onset Computer Co., MA, USA) was installed in the experimental area and hourly wind speed, precipitation, air temperature, relative humidity and solar radiation were collected. As shown in Table 1, air temperature, relative humidity and wind speed were obtained from a hand-held weather meteorograph, and solar radiation was obtained from the weather station.

2.4. Model establishment and accuracy evaluation

2.4.1. Calculation of water deficit indices

To build the water regime training and testing models for wheat from separate datasets, the GS at each growth stage in the two-year experiment was normalized as NGS (Eq. 5).

$$NGS_i = \frac{GS_i}{GS_{\max}} \tag{5}$$

Where GS_{max} is the maximum value of GS measured in each growing season (547.5 mmol m^{-2} s^{-1} in 2021 and 575.4 mmol m^{-2} s^{-1} in 2022).

The effective soil water content (EWC) in the soil that can be utilized by crops was calculated as Eq. 6:

$$EWC_i = \frac{SWC_i - WP}{FC_i - WP} \tag{6}$$

Where FC_i is the field capacity of 0–40 cm soil layer of each plot (ranging from 0.21 to 0.24 cm^3 cm^{-3}) and WP is the wilting point (WP=0.05 cm^3 cm^{-3}).

2.4.2. Machine learning modelling

Due to the high collinearity between the vegetation indices, a Principal Component Analysis (PCA) was performed to reduce the dimensions (Abdi and Williams, 2010). The PCA was performed on the VIs and TIs measured in two years at each growth stage to determine important variables and the relationship between VIs and TIs. The PCA axes with a cumulative contribution rate of principal component variance above 98% were used as inputs of the winter wheat water stress prediction models.

Three different machine learning algorithms were evaluated. PLS (Partial Least Squares) is a multivariate statistical data analysis method that combines the advantages of principal component analysis, canonical correlation analysis, and linear regression analysis (Abdi, 2010). SVM (Support Vector Machines) is a supervised machine learning algorithm that implements classification and regression by constructing a hyperplane or set of hyperplanes in a high-dimensional or infinite-dimensional space (Cortes et al., 1995). GBDT (Gradient Boosted Decision Trees) is a commonly used ensemble learning algorithm. This algorithm trains multiple individual learners, and then combines them through certain strategies to form a strong learner, which has the characteristics of high fitting accuracy and strong interpretability (Friedman, 2002). In this study, the number of iterations of GBDT was chosen as 100, and the learning rate was 0.1. The maximum depth of the regression tree was 7, the minimum number of leaf nodes samples was 5, and the maximum number of features was 3.

The Principal Components (PCs) calculated for each growth stage in 2021 were used as input to build NGS and EWC prediction models. To verify the applicability of the model, the PCs in 2022 for each growth stage were used to test the performance of the models. In addition, a separate analysis was performed in which the data of all different growth stages were pooled. We also constructed a separate model for pre-heading (tillering, jointing and booting stage) and post-heading stage (heading, flowering and filling stage). Finally, to compare the impact of multispectral and thermal images on the prediction accuracy of winter wheat growth parameters, models using only multispectral vegetation indices (VIs) were included as input, or using both VIs and thermal-based indices (VIs + TIs) were included.

2.4.3. Statistical analysis

The coefficient of determination (R^2), root mean square error (RMSE), and normalized root mean square error (NRMSE) from Eqs. 7–9 were used to evaluate the reliability and accuracy of the models' prediction results. Statistically, the higher R^2 and the smaller RMSE and NRMSE, the higher the accuracy of a prediction model. The simulation effect evaluation was divided into four levels according to the NRMSE: excellent (NRMSE $\leq$ 10%), good (10% < NRMSE $\leq$ 20%), suitable (20% < NRMSE $\leq$ 30%), and poor (NRMSE > 30%). A schematic illustrating the methodology is presented in Fig. 3.

$$R^2 = 1 - \frac{\sum_{i=1}^{n}(y_i - \hat{y}_i)^2}{\sum_{i=1}^{n}(y_i - \overline{y_i})^2} \tag{7}$$

$$RMSE = \sqrt{\frac{1}{n}\left(\sum_{i=1}^{n}(y_i - \hat{y}_i)^2\right)} \tag{8}$$

$$NRMSE = \frac{\sqrt{\frac{1}{n}\sum_{i=1}^{n}(y_i - \hat{y}_i)^2}}{\overline{y}} \times 100\% \tag{9}$$

Where y_i is measured value of NGS or EWC, $\hat{y}_i$ is predicted value of NGS or EWC, $\overline{y}$ is average measured value of NGS or EWC, n is number of samples.

3. Results

3.1. Statistics of NGS and EWC of wheat under different irrigation treatments

Fig. 4(a) and (b) show the variation of NGS and EWC of wheat under the different irrigation deficit treatments. In the tillering stage, the difference in NGS and EWC between the different treatments was still limited (ranging from 0.28 to 0.37 in 2021 and from 0.27 to 0.41 in 2022 for NGS, and from 0.36 to 0.42 in 2021 and from 0.34 to 0.41 in 2022 for EWC, respectively). With the growth of wheat, these differences between irrigation treatments gradually increased, peaking in the flowering (NGS) and filling stages (EWC). The two-year experimental results have high synergy, which provided a favorable data set for the testing of the model.

Linear regression models of each growth stage showed the close

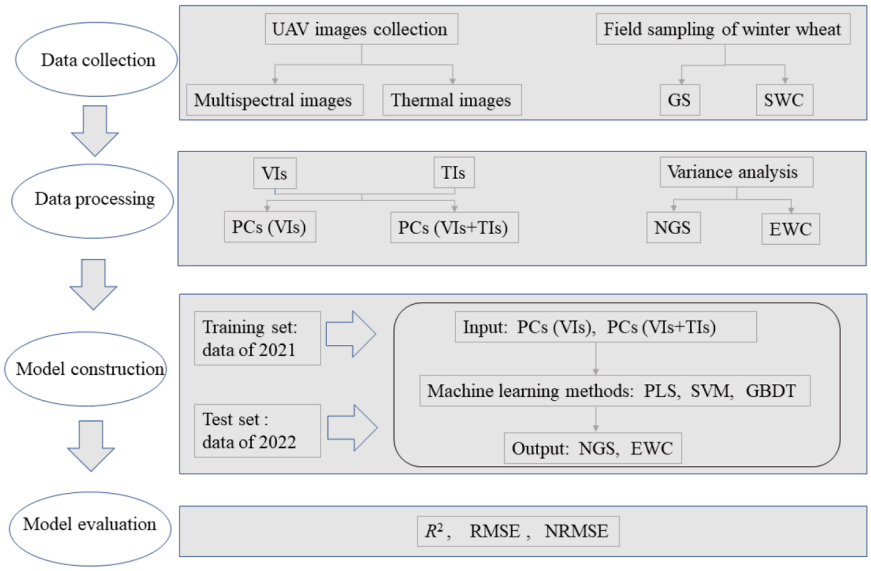

Fig. 3. Flowchart showing the experimental methodology. VIs, vegetation indices; TIs, thermal indices; PCs, principal components; GS, stomatal conductance; SWC, soil water content; NGS, normalized stomatal conductance; EWC, effective water content; PLS, partial least squares; SVM, support vector machine; GBDT, gradient boosting decision tree; R^2, coefficient of determination; RMSE, root mean square error; NRMSE, normalized root mean square error.

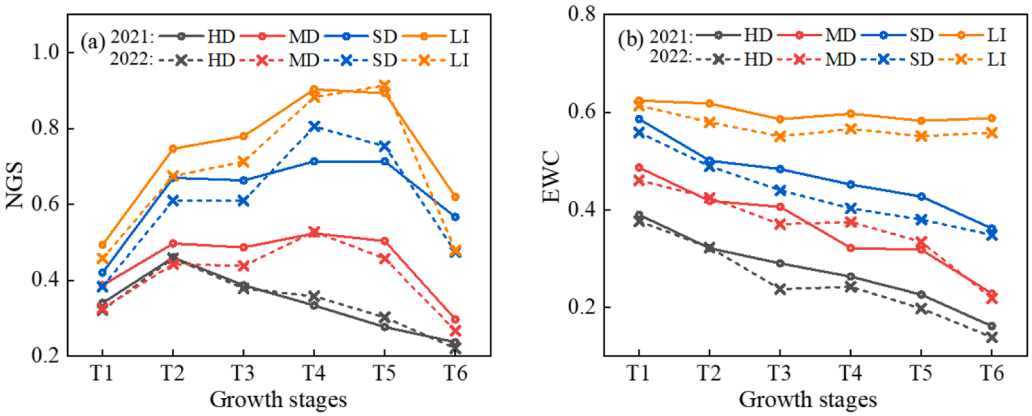

Fig. 4. NGS (a) and EWC(b) under different irrigation treatments. NGS and EWC represent normalized stomatal conductance and effective water content, respectively. HD, MD, SD and LI represent high deficit, moderate deficit, slight deficit and local irrigation, respectively. T1 to T6 represent the growth stage of tillering, jointing, booting, heading, flowering, and filling, respectively.

correlation between NGS and EWC (Fig. 5). Under water stress conditions, the transpiration rate of wheat decreased, so NGS decreased with the decrease of EWC. However, the regression models of the six growth stages were different. In the tillering and jointing stages, R^2 varied slightly between 0.65 and 0.68. R^2 increased significantly in booting and heading stages. For both years, the correlations were strongest at the flowering stage.

3.2. Relationships between VIs, TIs and water stress levels

The Pearson correlation coefficient matrix of on the one hand NGS and EWC and on the other hand the VIs and TIs at different growth stages is given in Fig. 6. All VIs except SIPI (structure insensitive pigment index) were positively correlated with NGS and EWC, whereas SIPI, △T, and CWSI were negatively correlated with these two variables. To clearly distinguish the correlation between the spectral variables and the canopy temperature indices with the two variables, the correlation coefficient r was taken as the absolute value(| r |) for analysis, and the following correlation coefficients were referred to | r | .

In the tillering stage, △T and CWSI had the highest correlation with NGS, while RVI (ratio vegetation index), NDVI, and GOSAVI (green optimal soil adjusted vegetation index) also showed good correlations with NGS. △T and CWSI also performed best in jointing and booting stages, followed closely by MSR (modified simple ratio index), RVI and NDVI. Some differences between both years were found in the heading stage, where MSR, RVI and NDVI were highly correlated with NGS in 2021, whereas △T and CWSI were most highly correlated with NGS in 2022. At flowering and filling stages, RVI, CIRE (red-edge chlorophyll index), MSR and RERVI (red-edge vegetation index) correlated most closely with NGS. Overall, RVI had the highest correlation throughout the entire growing season, for both years, closely followed by CWSI.

The correlations between EWC, and VIs and TIs were slightly lower than those of NGS. In tillering and jointing stages, △T and CWSI were most highly correlated with EWC. However, RVI, MSR and GNDVI (green normalized difference vegetation index) showed a higher correlation with EWC than TIs in booting, heading and flowering stages. At filling stage, RVI and NDVI performed best in 2021and 2022, respectively. In summary, the correlation between TIs and NGS and EWC was slightly better than that of the VIs in the early growth stages, but this was less obvious in the late growth stages. Still, overall, CWSI was the most

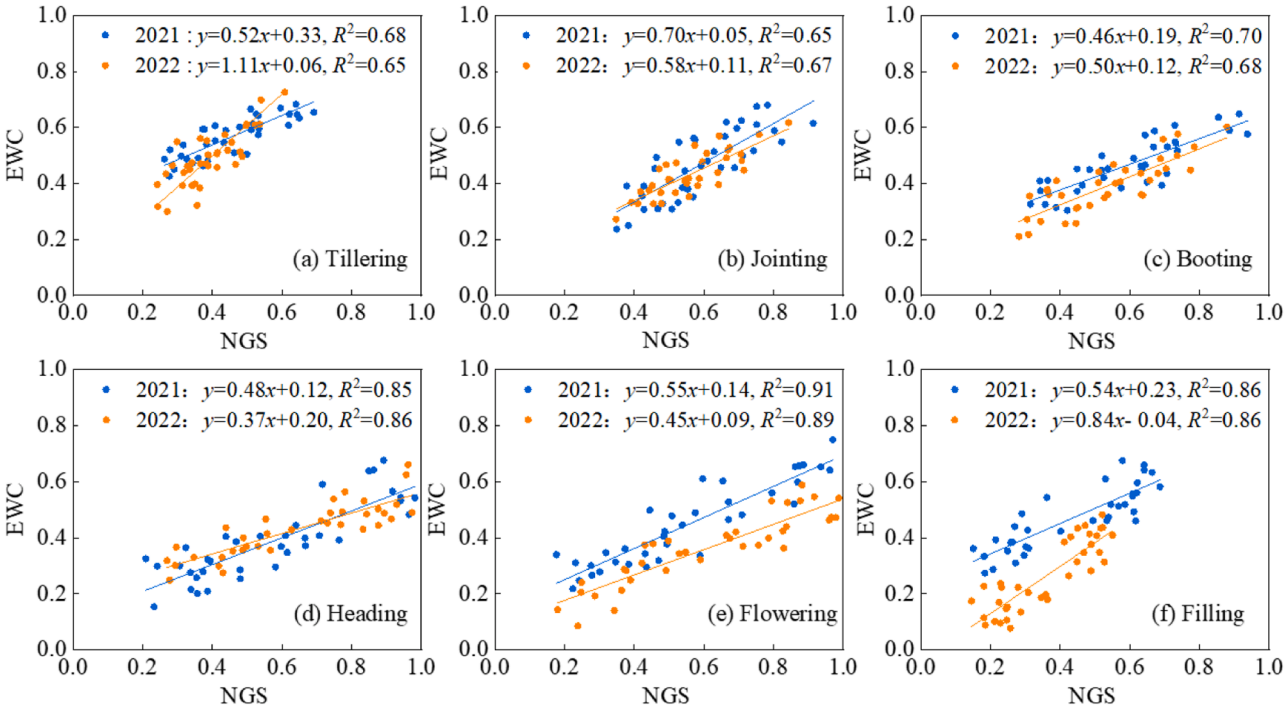

Fig. 5. Correlation between EWC and NGS at different growth stages. NGS and EWC represent normalized stomatal conductance and effective water content, respectively.

highly correlating variable throughout the entire season, and for both years. During the whole experimental period, VIs of RVI, MSR, and NDVI performed well with NGS and EWC.

3.3. Principal Components of PCA with VIs and VIs+TIs

Fig. 7 shows the cumulative contribution of the PCs in the PCA analyses by VIs (a) and VIs+TIs (b). The cumulative contribution of the top 4 PCA components reached over 98% for all PCA analyses. Therefore, we consider it appropriate to use 4 PCA components for VIs and VIs + TIs in this study to model NGS and EWC (Section 3.4 & 3.5).

For the PCA on the VIs, 93.5% of the variation was explained by the first two components, in both pre-heading and post-heading stages. In the pre-heading stage, OSAVI (optimized soil adjusted vegetation index), GOSAVI, NDVI and NDRE (normalized difference red-edge) were strongly positively and SIPI strongly negatively correlated with PC1, with EVI (enhanced vegetation index) more correlated with PC2 (Fig. 8a). In the post-heading stage (Fig. 8b), the overall correlation pattern between the individual VIs was very similar, although they were less strongly correlated to PC1. The two first PC of the PCA on the VIs + TIs explained 85.7% and 87.6% of the variation in pre-heading and post-heading stages, respectively. In the pre-heading stage (Fig. 8c), nearly all VIs were very strongly correlated to PC1, and the two TIs to PC2. In the post-heading stage (Fig. 8d), the TIs were strongly correlated with several VIs (e.g., △T with SIPI, MSR and RVI; CWSI with GNDVI and NDRE). Consequently, both TIs were negatively correlated with PC1 and the PCA of VIs + TIs closely resembled the PCA of the VIs in this stage (Figs. 8b and 8d).

3.4. Models simulating NGS

The 4 PCA axes from VIs and VIs + TIs were used as input variables to construct NGS prediction models with PLS, SVM, and GBDT. This section only shows the results of the test set; the results of the training set can be found in the Appendix (Table A.1). The accuracy of the NGS prediction models varied at different growth stages (Fig. 9). None of the models performed well at tillering stage, but the model accuracy gradually increased for the jointing, booting, and heading stages. The prediction accuracy peaked at the flowering stage ($R^2 > 0.80$) and decreased during the filling stage. Combining all data from the pre-heading stage into a single model clearly increased the model performance, although overall performance was still lower (R^2 =0.65–0.75) than that of the post-heading stage (R^2 =0.84–0.88).

Compared to VIs, the combination of VIs and TIs consistently improved the prediction accuracy of NGS at all stages. R^2 values improved from 0.74 to 0.79 at pre-heading stage and from 0.87 to 0.90 at post-heading stage for the GBDT method.

Among the three methods, PLS usually performed slightly worse, particularly in the early and later growth stages. For the individual growth stages, GBDT and SVM performed similarly. However, the GBDT model performed consistently best for the aggregate pre-heading and post-heading models.

3.5. Models simulating EWC

With the aim of assessing the spatial variability of soil water availability in the large-scale field, this study constructed EWC prediction models by combining SWC, FC, and WP for the soil layers from 0 to 40 cm. The results of the training set can be found in Appendix (Table A.2), and the results of the independent test dataset are shown in Fig. 10. The results show large similarity with those of the NGS models: combining VIs and TIs consistently improved model performance, and the models of pre-heading and post-heading reached a good level (10% < NRMSE ≤ 20%), with the post-heading model performing slightly better than the pre-heading model. The ensemble model in the pre-heading stage performed better than the individual stage models. PLS models had the lowest accuracy, and GBDT models overall had the highest accuracy. R^2 was lower and RMSE and NRMSE were higher at the tillering and jointing stages. Different from the NGS models, the models achieved the best results in filling stage, with GBDT (R^2 = 0.90, RMSE = 0.05, NRMSE = 15.9%) as the best model.

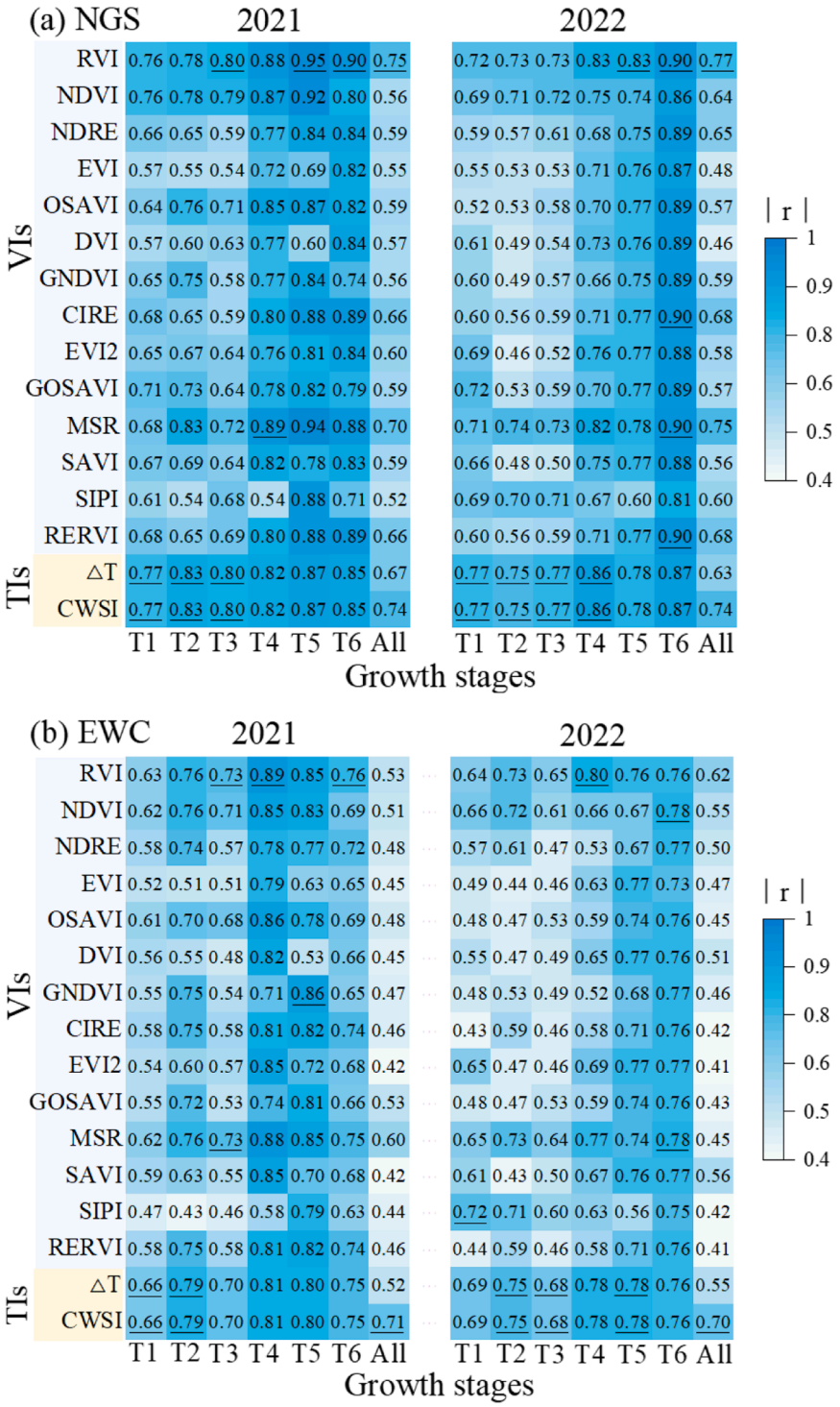

Fig. 6. Absolute value of the Pearson correlation coefficient | r | of the vegetation indices (VIs) and thermal indices (TIs) with the normalized stomatal conductance (NGS) (a) and the effective soil water content (EWC) (b) at different growth stages. T1 to T6 represent the growth stage of tillering, jointing, booting, heading, flowering and filling, respectively. 'All' represents all growth stages from T1 to T6. RVI, NDVI, NDRE, EVI, OSAVI, DVI, GNDVI,CIRE, EVI2, GOSAVI, MSR, SAVI, SIPI and RERVI represent ratio vegetation index, normalized difference vegetation index, normalized difference red-edge, enhanced vegetation index, optimized soil adjusted vegetation index, difference vegetation index, green normalized difference vegetation index, red-edge chlorophyll index, enhanced vegetation index, green optimal soil adjusted vegetation index, modified simple ratio index, soil adjusted vegetation index, structure insensitive pigment index and red-edge vegetation index, respectively. △T and CWSI represent the difference between canopy temperature and air temperature, and crop water stress index, respectively.

4. Discussion

The GS and SWC are important indicators for characterizing crop water stress. Large-scale monitoring of crop water status based on UAV remote sensing technology is greatly important for wheat management. In this study, prediction models of NGS and EWC were constructed using VIs and TIs calculated from UAV spectral and thermal remote sensing to evaluate water stress of winter wheat.

As expected, △T and CWSI were indeed more highly correlated with NGS and EWC than the VIs in the early growth stages, when the growth

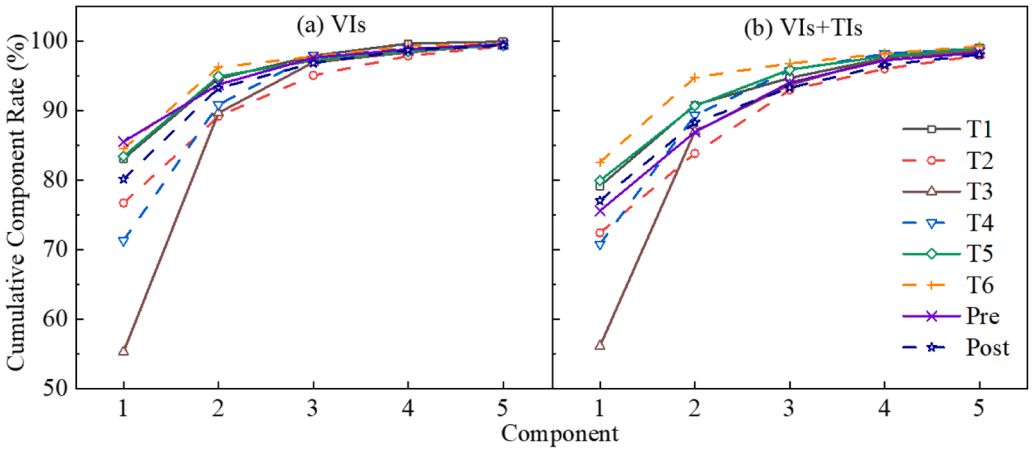

Fig. 7. Cumulative contribution rate of each component of principal component analysis for VIs (a) and VIs+TIs (b) by combining 2021 and 2022. T1 to T6 represent the growth stage of tillering, jointing, booting, heading, flowering and filling, respectively. Pre and post represent pre-heading stage and post-heading stage, respectively.

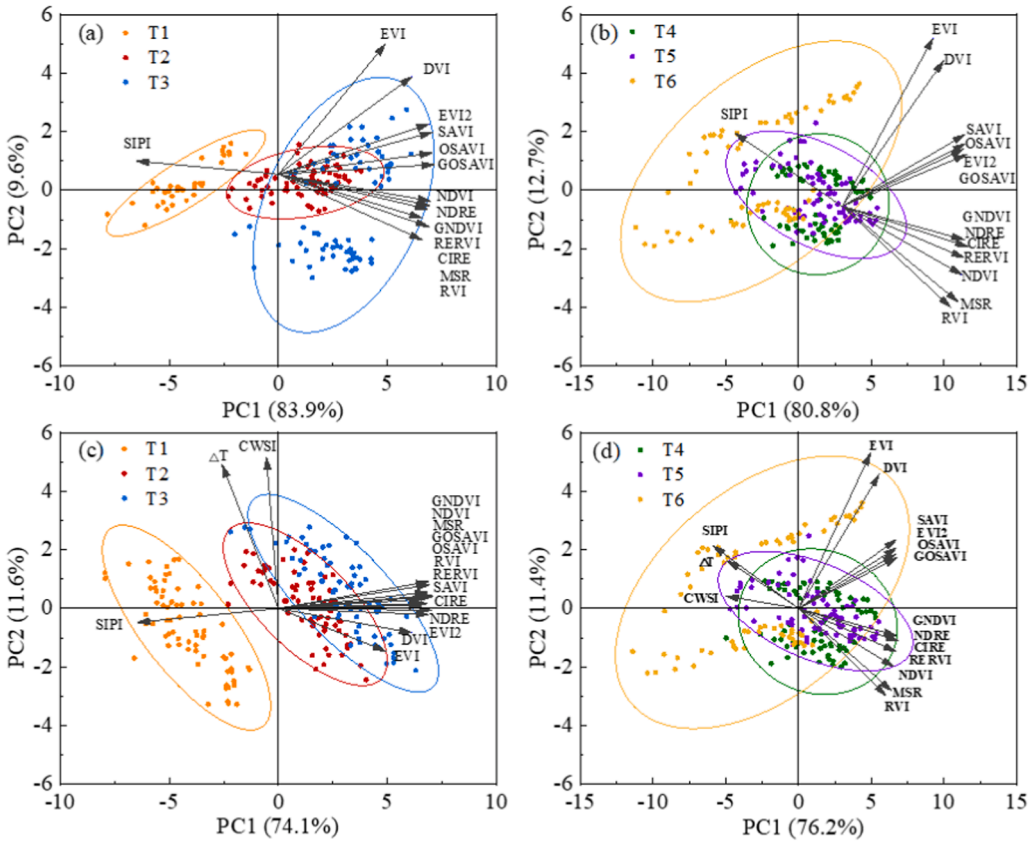

Fig. 8. The two first principal component axes of the Principal Component Analysis (PCA) performed on the vegetation indices and thermal indices (△T and CWSI) at different growth stages by combining 2021 and 2022. PCA results of VIs at pre-heading stage (T1, T2 and T3 represent the growth stage of tillering, jointing, and booting, respectively.) (a) and post-heading stage (T4, T5 and T6 represent the growth stage of heading, flowering, and filling, respectively.) (b). PCA results of combining VIs and TIs at pre-heading stage (c) and post-heading stage (d). RVI, NDVI, NDRE, EVI, OSAVI, DVI, GNDVI,CIRE, EVI2, GOSAVI, MSR, SAVI, SIPI and RERVI represent ratio vegetation index, normalized difference vegetation index, normalized difference red-edge, enhanced vegetation index, optimized soil adjusted vegetation index, difference vegetation index, green normalized difference vegetation index, red-edge chlorophyll index, enhanced vegetation index, green optimal soil adjusted vegetation index, modified simple ratio index, soil adjusted vegetation index, structure insensitive pigment index and red-edge vegetation index, respectively. △T and CWSI represent the difference between canopy temperature and air temperature, and crop water stress index, respectively.

of the plants did not yet differ much between the treatments. Still, this study revealed that in the later growth stages, several VIs (e.g., RVI, RERVI and MSR) were even more closely correlated with NGS and EWC than the TIs.

Following the lower correlation of VIs with NGS and EWC in the early stages, the performance of the models predicting the water stress variables was lower, particularly when only VIs were used as input (Figs. 9 and 10). This study confirmed that the prediction accuracy of combining VIs and TIs by PCA as input was higher than when relying only on multispectral data. This is consistent with findings by Cheng

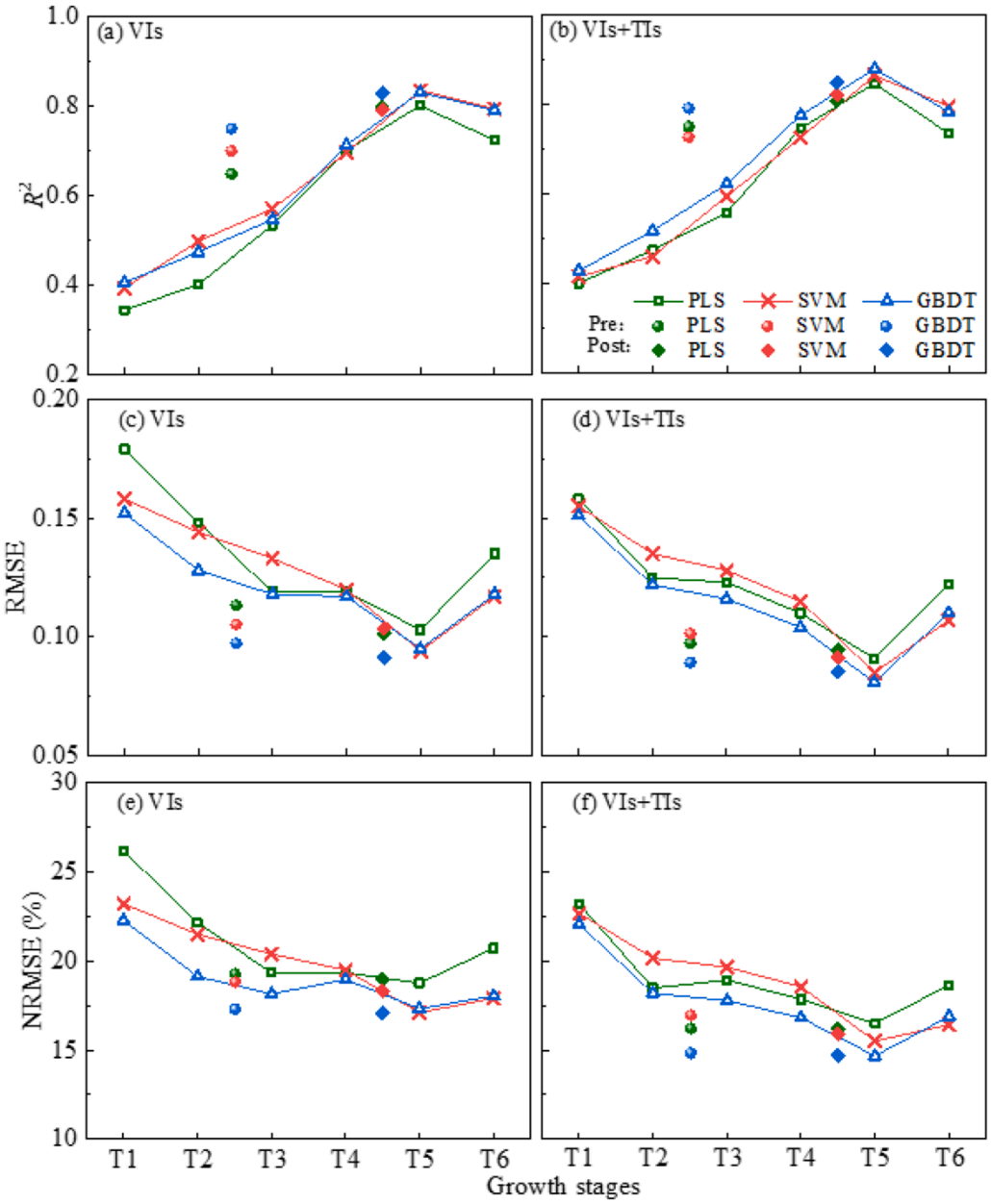

Fig. 9. Results of the independent test dataset (data of 2022) of NGS with VIs (a, c and e) and VIs+TIs (b, d and f). VIs and TIs represent vegetation indices and thermal indices, respectively. PLS, SVM and GBDT represent machine learning methods of partial least squares, support vector machine and gradient boosting decision tree, respectively. T1 to T6 represent the growth stage of tillering, jointing, booting, heading, flowering, and filling, respectively. Pre and Post represent pre-heading stage and post-heading stage, respectively.

et al. (2022) who predicted the soil water content in corn. Our study confirmed that the combination of multispectral and canopy temperature image datasets for water stress monitoring at key growth stages improved the accuracy of predictive models. Another study indicated that WDI derived from multispectral and thermal sensors is a reliable factor in assessing the water status of winter wheat (Antoniuk et al., 2023). Specifically, the WDI had a consistently high correlation with GS during the whole season (R^2 ranged from 0.63 to 0.99). But their study lacked a truly independent test set, so the applicability of the model in different growth seasons still needs to be verified.

In our study, the prediction accuracy of the NGS model first increased and then decreased with the growth of wheat, with optimal performance at flowering stage, in line with models predicting GS by Zhou et al. (2021), using solely multispectral remote sensing. However, the prediction accuracy of the EWC model showed a gradually increasing trend with the growth of wheat. This is probably because in the late stages of the growing season, SWC remained stable, whereas GS dropped during the filling stage (Figs. 6 and 7). This decrease during filling stage can be attributed to the weakening of leaf vitality (Xue et al., 2006). Conversely, the accumulated drought stress widened the gap of SWC between different irrigation treatments at filling stage. The accuracy of the models predicting NGS was overall higher than those targeting EWC. GS is a more direct indicator of plant water status and hence more closely related to VIs and TIs than SWC (Jones, 2004).

Similar to the findings of Zia et al. (2012), the models showed better performance in the post-heading than in the pre-heading stage. An interesting observation was that the ensemble pre-heading model performed better than the individual models in the tillering, jointing and booting stages, while the ensemble model accuracy of post-heading was not significantly improved. This may be due to the gradual growth of

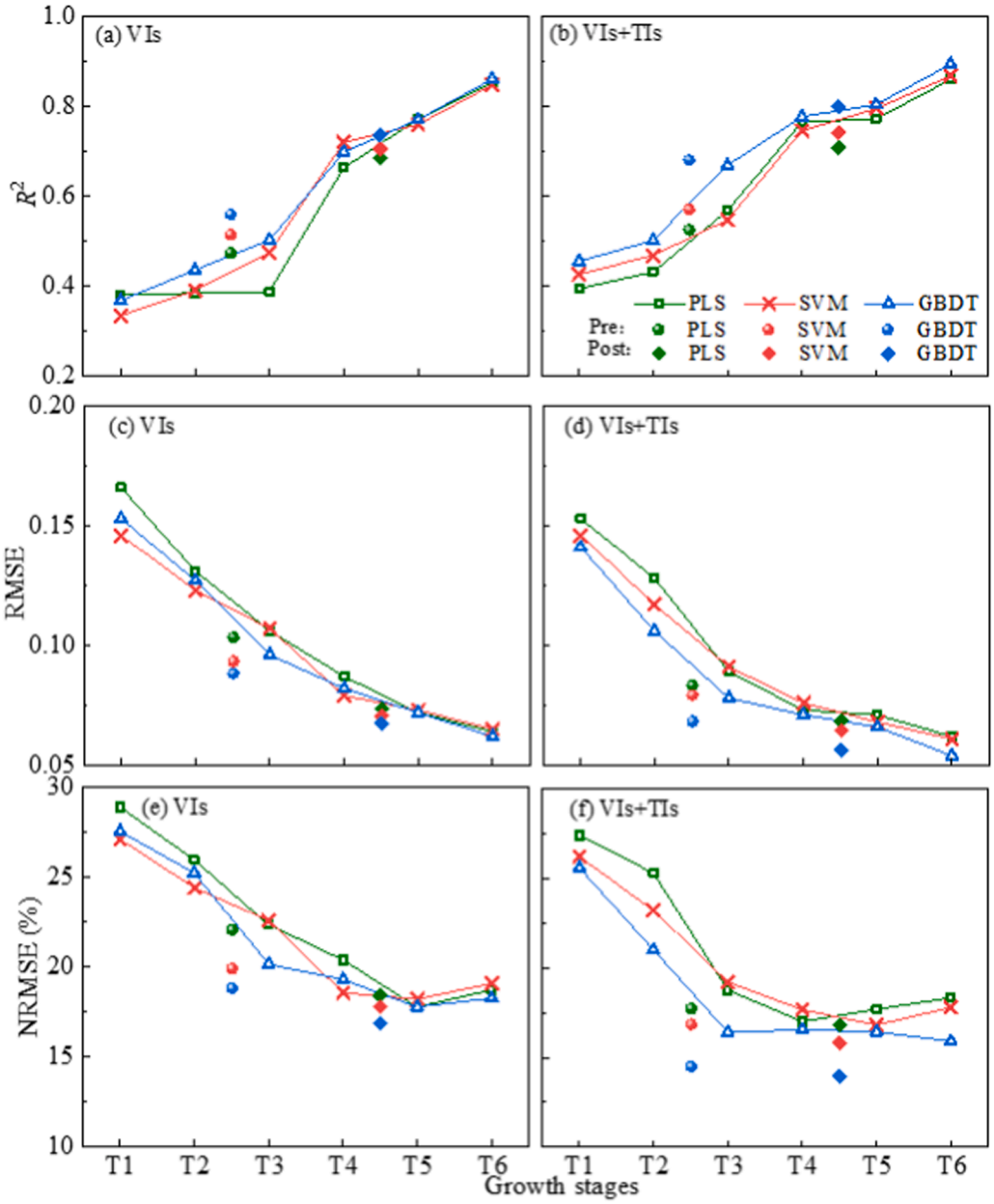

Fig. 10. Results of the test set of EWC with VIs (a, c and e) and VIs+TIs (b, d and f). VIs and TIs represent vegetation indices and thermal indices, respectively. PLS, SVM and GBDT represent machine learning methods of partial least squares, support vector machine and gradient boosting decision tree, respectively. T1 to T6 represent the growth stage of tillering, jointing, booting, heading, flowering, and filling, respectively. Pre and Post represent pre-heading stage and post-heading stage, respectively.

wheat before heading, which increases the canopy coverage. The results indicate that in the early stages, the relationship between on the one hand NGS, EWC and on the other hand VIs and TIs remains relatively stable. Technically, a model incorporating more data (from different growth stages) is more robust.

Overall, the GBDT model outperformed the PLS and SVM models with higher R^2, lower RMSE and NRMSE in NGS and EWC estimation for most of the wheat growth stages. This is in line with recent research that also found high precisions for the GBDT algorithm (Du et al., 2022; Fan et al., 2018). GBDT is an ensemble algorithm based on decision trees. Its basic learner is serially generated, that is, each new learner generated is based on the previous modeling results. Therefore, it can be used as a good single regression model, providing very robust prediction, excellent and stable model discrimination ability. The generated new learners are based on the previous modeling results (Obsie et al., 2020). In addition, each decision tree of GBDT only learns the prediction residual part of the observation data, which is less prone to over-fitting. The SVM can solve nonlinear problems by introducing kernel functions. Although it also shows high test set accuracy in some growth stages, the fitting accuracy was not as good as the GBDT method from the perspective of the entire growth seasons. PLS performed the worst, probably because it cannot handle the non-linear problem in water stress prediction well.

These data were analyzed based on the four irrigation treatment levels, six growth stages, and two growing seasons. A completely independent data set, collected in a separate year, was used as test dataset. The results showed that the both models reached a good level, indicating the stability of the ensemble approaches on new data. Zhou et al. (2021) built a GS prediction model of winter wheat with R^2 greater than 0.80 by combining the multispectral vegetation indices and texture features. However, the study used the dataset of the flowering stage of a single

growing season for training and testing of the model. Similarly, Qin et al. (2022) and Cheng et al. (2022) built predictive models for wheat GS and maize SWC respectively, but no truly independent dataset was used in their research. Our model results can be used in other growth seasons or independent datasets to diagnose water stress in wheat. In addition, compared with the single growth stage, two independent models (pre-heading and post-heading stage) achieved acceptable test set results, which provided a reference for irrigation plans. These models can reliably estimate NGS and EWC without the need to define the growth stage in detail. Therefore, modelling NGS and EWC for wheat at these two growth periods is straightforward, without requiring models for each growth stage. In addition, this study accurately controlled the amount of irrigation in the two growing seasons, thereby expanding the range of NGS and EWC, and achieving good test set results.

Despite the independent dataset gathered in a separate year, the current study was performed within a single field and with a single variety of wheat. Different varieties of wheat as well as differences in climate and soil characteristics could affect the relationship between VIs, TIs and stomatal control. Hence, future studies should focus on implementing the models that combine multiple sites and varieties to extend those outcomes. Nonetheless, the determination of crop surface canopy temperature for both severely stressed and unstressed plants was ascertained by analyzing the 1 % and 99 % quantiles of the thermal image's histogram captured on the respective flying day. However, it should be acknowledged that this simplified methodology may not be universally applicable, particularly in cases where vegetated areas do not exhibit pronounced water deficiency. This limitation arises from the inherent inability to establish a baseline for CWSI. The OTSU was employed to segregate the vegetation from the soil background. However, a comprehensively comparative analysis of the impact of distinct methodologies on model accuracy was not compared in this study. Furthermore, sandy soil, such as presentin the experimental site, drains faster than loamy or clay soil. Consequently, the canopy temperature of sandy soil tends to exhibit higher temperatures under water stress conditions. In prospective investigations, the best method for distinguishing between soil and vegetation in sandy soils should be studied. This refinement will enable better application of histogram analysis to discriminate between non-transpiring and fully transpiring crops. Additionally, wheat water deficit diagnostic models were constructed based solely on UAV multispectral and thermal remote sensing. For precision irrigation, winter wheat water stress map (Fig. 11) still needs to be converted into a task map of irrigation requirements, for which it is also necessary to include climatic conditions or soil properties in the decision process.

5. Conclusions

A two-year winter wheat water deficit field experiment was conducted. The stomatal conductance and soil water content during the critical growth stages of wheat were monitored, and the water stress of wheat was assessed based on UAV multispectral and thermal remote sensing. The results showed that temperature indices (TIs, $\triangle$T and CWSI) had a higher correlation with normalized stomal conductance (NGS) and effective water content (EWC) in the early growth stage, while RVI, CIRE, MSR, GNDVI, and RERVI from vegetation indices (VIs) performed better in the late growth stage. In this study, data from different growing seasons were used to construct the training and testing sets of the model. The gradient boosting decision tree (GBDT) method exhibited higher performance compared to partial least squares (PLS) and support vector machine (SVM), and the NGS could be better predicted than EWC. Combining VIs and TIs effectively improved the prediction accuracy of the NGS and EWC models. R^2 increased from 0.83 to 0.88 (NGS) and 0.77–0.81 (EWC) at the flowering stage by GBDT method. Overall, this study provides robust models to diagnose water deficit comprehensively and accurately in winter wheat using UAV remote sensing.

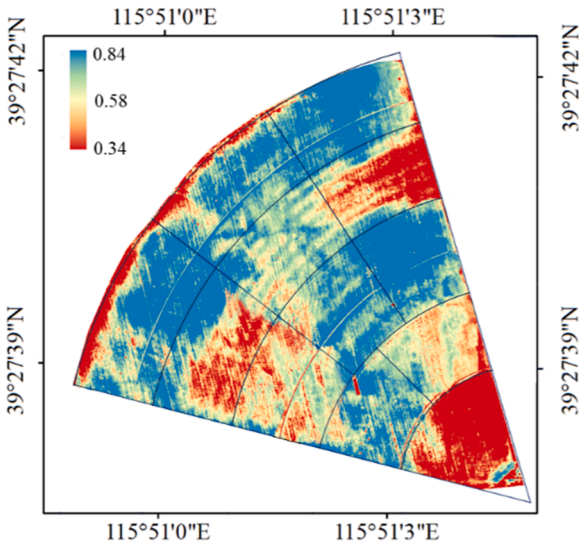

Fig. 11. Water stress map of NGS at the flowering stage in 2022.

CRediT authorship contribution statement

Hui Xin: Resources, Methodology, Conceptualization. **Zhang Haohui:** Methodology, Investigation. **Lou Yu:** Methodology, Investigation. **Wang Jingjing:** Writing – review & editing, Writing – original draft, Software, Resources, Methodology, Investigation. **Liu Suyi:** Software, Formal analysis, Data curation. **Wang Wentao:** Software, Investigation. **Maes Wouter:** Writing – original draft, Supervision. **Yan Haijun:** Writing – review & editing, Writing – original draft, Supervision, Resources, Funding acquisition. **Wang Yunling:** Validation, Software, Methodology.

Declaration of Competing Interest

The authors declare that they have no known competing financial interests or personal relationships that could have appeared to influence the work reported in this paper.

Data Availability

Data will be made available on request.

Acknowledgements

We would like to thank the China Scholarship Council (CSC) for financially supporting to the first author. The authors are greatly indebted to the Key Research and Development Program of Hebei Province (Grant No. 21327002D), Water Conservancy Technology Demonstration Project of Ministry of Water Resources of China (Grant No. SF-202311) and China Agriculture Research System (Grant No. CARS-03).

Appendix A. Supporting information

Supplementary data associated with this article can be found in the online version at doi:10.1016/j.agwat.2023.108616.

References

Abdi, H., 2010. Partial least squares regression and projection on latent structure regression (PLS Regression). Wiley Inter. Rev. Comput. Stat. 2, 97–106. https://doi.org/10.1002/wics.51.

Abdi, H., Williams, L.J., 2010. Principal component analysis. Wiley Inter. Rev. Comput. Stat. 2, 433–459. https://doi.org/10.1002/wics.101.

Abioye, E.A., Abidin, M.S.Z., Mahmud, M.S.A., Buyamin, S., Ishak, M.H.I., Rahman, M.K. I.A., Otuoze, A.O., Onotu, P., Ramli, M.S.A., 2020. A review on monitoring and advanced control strategies for precision irrigation. Comput. Electron Agric. 173, 105441 https://doi.org/10.1016/j.compag.2020.105441.

Abuzar, M., O'Leary, G., Fitzgerald, G., 2009. Measuring water stress in a wheat crop on a spatial scale using airborne thermal and multispectral imagery. Field Crops Res. 112, 55–65. https://doi.org/10.1016/j.fcr.2009.02.001.

Antoniuk, V., Zhang, X., Andersen, M.N., Kørup, K., Manevski, K., 2023. Spatiotemporal winter wheat water status assessment improvement using a water deficit index derived from an unmanned aerial system in the North China Plain. Sensors 23. https://doi.org/10.3390/s23041903.

Bhandari, M., Baker, S., Rudd, J.C., Ibrahim, A.M.H., Chang, A., Xue, Q., Jung, J., Landivar, J., Auvermann, B., 2021. Assessing the effect of drought on winter wheat growth using unmanned aerial system (UAS)-based phenotyping. Remote Sens. (Basel) 13. https://doi.org/10.3390/rs13061144.

Bhattarai, N., Wagle, P., Gowda, P.H., Kakani, V.G., 2017. Utility of remote sensing-based surface energy balance models to track water stress in rain-fed switchgrass under dry and wet conditions. ISPRS J. Photo 133, 128–141. https://doi.org/10.1016/j.isprsjprs.2017.10.010.

Broge, N.H., Mortensen, J.V., 2002. Deriving green crop area index and canopy chlorophyll density of winter wheat from spectral reflectance data. Remote Sens. Environ. 81, 45–57. https://doi.org/10.1016/S0034-4257(01)00332-7.

Buckley, T.N., 2019. How do stomata respond to water status? N. Phytol. 224, 21–36. https://doi.org/10.1111/nph.15899.

Cao, Q., Miao, Y., Wang, H., Huang, S., Cheng, S., Khosla, R., Jiang, R., 2013. Non-destructive estimation of rice plant nitrogen status with Crop Circle multispectral active canopy sensor. Field Crops Res. 154, 133–144. https://doi.org/10.1016/j.fcr.2013.08.005.

Cao, Q., Miao, Y., Feng, G., Gao, X., Li, F., Liu, B., Yue, S., Cheng, S., Ustin, S.L., Khosla, R., 2015. Active canopy sensing of winter wheat nitrogen status: An evaluation of two sensor systems. Comput. Electron Agric. 112, 54–67. https://doi.org/10.1016/j.compag.2014.08.012.

Cheng, M., Jiao, X., Liu, Y., Shao, M., Yu, X., Bai, Y., Wang, Z., Wang, S., Tuohuti, N., Liu, S., Shi, L., Yin, D., Huang, X., Nie, C., Jin, X., 2022. Estimation of soil moisture content under high maize canopy coverage from UAV multimodal data and machine learning. Agric. Water Manag. 264 https://doi.org/10.1016/j.agwat.2022.107530.

Cortes, C., Vapnik, V., Saitta, L., 1995. Support-vector networks. Mach. Learn 20, 273–297. https://doi.org/10.1007/BF00994018.

Daccache, A., Knox, J.W., Weatherhead, E.K., Daneshkhah, A., Hess, T.M., 2015. Implementing precision irrigation in a humid climate - recent experiences and on - going challenges. Agric. Water Manag. 147, 135–143. https://doi.org/10.1016/j.agwat.2014.05.018.

Daniels, L., Eeckhout, E., Wieme, J., Dejaegher, Y., Audenaert, K., Maes, W.H., 2023. Identifying the Optimal Radiometric Calibration Method for UAV-Based Multispectral Imaging. Remote Sens ((Basel). 15.). https://doi.org/10.3390/rs15112909.

Das, S., Christopher, J., Roy Choudhury, M., Apan, A., Chapman, S., Menzies, N.W., Dang, Y.P., 2022. Evaluation of drought tolerance of wheat genotypes in rain-fed sodic soil environments using high-resolution UAV remote sensing techniques. Biosyst. Eng. 217, 68–82. https://doi.org/10.1016/j.biosystemseng.2022.03.004.

De Swaef, T., Maes, W.H., Aper, J., Baert, J., Cougnon, M., Reheul, D., Steppe, K., Roldán-Ruiz, I., Lootens, P., 2021. Applying rgb-and thermal-based vegetation indices from UAVs for high-throughput field phenotyping of drought tolerance in forage grasses. Remote Sens. (Basel) 13, 1–24. https://doi.org/10.3390/rs13010147.

Du, Z., Yang, L., Zhang, D., Cui, T., He, X., Xiao, T., Xie, C., Li, H., 2022. Corn variable-rate seeding decision based on gradient boosting decision tree model. Comput. Electron Agric. 198 https://doi.org/10.1016/j.compag.2022.107025.

Ezenne, G.I., Jupp, L., Mantel, S.K., Tanner, J.L., 2019. Current and potential capabilities of UAS for crop water productivity in precision agriculture. Agric. Water Manag. 218 https://doi.org/10.1016/j.agwat.2019.03.034.

Fan, J., Yue, W., Wu, L., Zhang, F., Cai, H., Wang, X., Lu, X., Xiang, Y., 2018. Evaluation of SVM, ELM and four tree-based ensemble models for predicting daily reference evapotranspiration using limited meteorological data in different climates of China. Agric. Meteor. 263, 225–241. https://doi.org/10.1016/j.agrformet.2018.08.019.

FAO, 2023. Water Management. FAO, Rome, Italy. ⟨https://www.fao.org/land-water/water/water-management⟩.

Feng, L., Chen, S., Zhang, C., Zhang, Y., He, Y., 2021. A comprehensive review on recent applications of unmanned aerial vehicle remote sensing with various sensors for high-throughput plant phenotyping. Comput. Electron Agric. 182 https://doi.org/10.1016/j.compag.2021.106033.

Fitzgerald, G., Rodriguez, D., O'Leary, G., 2010. Measuring and predicting canopy nitrogen nutrition in wheat using a spectral index-the canopy chlorophyll content index (CCCI). Field Crops Res. 116, 318–324. https://doi.org/10.1016/j.fcr.2010.01.010.

Friedman, J.H., 2002. Stochastic gradient boosting. Comput. Stat. Data Anal. 38, 367–378. https://doi.org/10.1016/S0167-9473(01)00065-2.

Gago, J., Douthe, C., Coopman, R.E., Gallego, P.P., Ribas-Carbo, M., Flexas, J., Escalona, J., Medrano, H., 2015. UAVs challenge to assess water stress for sustainable agriculture. Agric. Water Manag. 153, 9–19. https://doi.org/10.1016/j.agwat.2015.01.020.

Gitelson, A.A., Kaufman, Y.J., Merzlyak, M.N., Blaustein, J., 1995. Use of a green channel in remote sensing of global vegetation from EOS-MODIS. Remote Sens. Environ. 58, 289–298. https://doi.org/10.1016/S0034-4257(96)00072-7.

Gitelson, A.A., Viña, A., Ciganda, V., Rundquist, D.C., Arkebauer, T.J., 2005. Remote estimation of canopy chlorophyll content in crops. Geophys Res. Lett. 32, 1–4. https://doi.org/10.1029/2005GL022688.

Haboudane, D., Miller, J.R., Pattey, E., Zarco-Tejada, P.J., Strachan, I.B., 2004. Hyperspectral vegetation indices and novel algorithms for predicting green LAI of crop canopies: Modeling and validation in the context of precision agriculture. Remote Sens. Environ. 90, 337–352. https://doi.org/10.1016/j.rse.2003.12.013.

Han, W., Zhang, L., Niu, X., Shi, X., 2020. Review on UAV remote sensing application in precision irrigation. Trans. Chin. Soc. Agric. 51 (2) https://doi.org/CNKI:SUN:NYJX.0.2020-02-001.

Huete, A.R., 1988. A soil-adjusted vegetation index (SAVI). Remote Sens. Environ. 25, 295–309. https://doi.org/10.1016/0034-4257(88)90106-X.

Hui, X., Lin, X., Zhao, Y., Xue, M., Zhuo, Y., Guo, H., Yan, H., 2022. Assessing water distribution characteristics of a variable-rate irrigation system. Agric. Water Manag. 260 https://doi.org/10.1016/j.agwat.2021.107276.

Jackson, R.D., Idso, S.B., Reginato, R.J., Pinter, P.J., 1981. Canopy temperature as a crop water stress indicator. Water Resour. Res. 17 (4), 1133–1138. https://doi.org/10.1029/WR017i004p01133.

Jiang, Z., Huete, A.R., Didan, K., Miura, T., 2008. Development of a two-band enhanced vegetation index without a blue band. Remote Sens. Environ. 112, 3833–3845. https://doi.org/10.1016/j.rse.2008.06.006.

Jones, H.G., 2004. Irrigation scheduling: advantages and pitfalls of plant-based methods. J. Exp. Bot. 2427–2436. https://doi.org/10.1093/jxb/erh213.

Jordan, C.F., Jordan1, C.F., Rico, P., Center, N., Piedras, R., 1969. Derivation of leaf-area index from quality of light on the forest floor. Ecology 50, 660–663. ⟨https://www.jstor.org/stable/1936256⟩.

Kögler, F., Söffker, D., 2019. Explorative frequency analysis of leaf temperature behavior of maize (Zea mays subsp. mays) at water deficit. Plants 8. https://doi.org/10.3390/plants8040105.

Liu, H.Q., Huete, A., 2019. A feedback based modification of the NDVI to minimize canopy background and atmospheric noise. IEEE Trans. Geosci. Remote Sens. 33, 457–465. https://doi.org/10.1109/tgrs.1995.8746027.

Maes, W.H., Steppe, K., 2012. Estimating evapotranspiration and drought stress with ground-based thermal remote sensing in agriculture: a review. J. Exp. Bot. 63, 671–712. https://doi.org/10.1093/jxb/ers165.

Maes, W.H., Steppe, K., 2019. Perspectives for remote sensing with unmanned aerial vehicles in precision agriculture. Trends Plant Sci. 24, 152–164. https://doi.org/10.1016/j.tplants.2018.11.007.

Maes, W.H., Baert, A., Huete, A.R., Minchin, P.E.H., Snelgar, W.P., Steppe, K., 2016. A new wet reference target method for continuous infrared thermography of vegetations. Agric. Meteor. 226–227, 119–131. https://doi.org/10.1016/j.agrformet.2016.05.021.

Maes, W.H., Huete, A.R., Steppe, K., 2017. Optimizing the processing of UAV-based thermal imagery. Remote Sens. (Basel) 9. https://doi.org/10.3390/rs9050476.

Moran, M.S., Clarke, T.R., Inoue, Y., Vidal, A., 1994. Estimating crop water deficit using the relation between surface-air temperature and spectral vegetation index. Remote Sens. Environ. 49, 246–263. https://doi.org/10.1016/0034-4257(94)90020-5.

Obsie, E.Y., Qu, H., Drummond, F., 2020. Wild blueberry yield prediction using a combination of computer simulation and machine learning algorithms. Comput. Electron Agric. 178 https://doi.org/10.1016/j.compag.2020.105778.

Otsu, N., 1979. A threshold selection method from gray-level histogram. IEEE Trans. Sys 9, 62–66. https://doi.org/10.1109/TSMC.1979.4310076.

Penuelas, J., Frederic, B., Filella, I., 1995. Semi-empirical indices to assess Carotenoids/Chlorophyll-a ratio from leaf spectral reflectance diversity and ecosystem functions of boreal forest under global change view project Vegetation indices View project. Photosynthetica 31, 221–230. https://doi.org/10.1007/BF00029464.

Qin, W., Wang, J., Ma, L., Wang, F., Hu, N., Yang, X., Xiao, Y., Zhang, Y., Sun, Z., Wang, Z., Yu, K., 2022. UAV-based multi-temporal thermal imaging to evaluate wheat drought resistance in different deficit irrigation regimes. Remote Sens. (Basel) 14. https://doi.org/10.3390/rs14215608.

Reynolds, M.P., Braun, H.J., 2022. Wheat Improvement. Springer International Publishing. https://doi.org/10.1007/978-3-030-90673-3.

Rondeaux, G., Steven, M., Baret, F., 1996. Optimization of soil-adjusted vegetation indices. Remote Sens Environ. 55, 95–107. https://doi.org/10.1016/0034-4257(95)00186-7.

Rouse, R.W.H., Haas, J.A.W., Deering, D.W., 1974. Monitoring vegetation systems in the great plains with ERTS. Goddard Space Flight Center 3d ERTS-1 Symp. NASA, p. 1 https://doi.org/1974NASSP.351.309R.

Shirazi, M.A., Boersma, L., 1984. A unifying quantitative analysis of soil texture. SSSA J. 48 (1), 142–147. https://doi.org/10.2136/sssaj1984.03615995004800010026x.

Traore, A., Ata-Ul-karim, S.T., Duan, A., Soothar, M.K., Traore, S., Zhao, B., 2021. Predicting equivalent water thickness in wheat using UAV mounted multispectral sensor through deep learning techniques. Remote Sens. (Basel) 13. https://doi.org/10.3390/rs13214476.

Veysi, S., Naseri, A.A., Hamzeh, S., Bartholomeus, H., 2017. A satellite based crop water stress index for irrigation scheduling in sugarcane fields. Agric. Water Manag. 189, 70–86. https://doi.org/10.1016/j.agwat.2017.04.016.

Wang, X., Müller, C., Elliot, J., Mueller, N.D., Ciais, P., Jägermeyr, J., Gerber, J., Dumas, P., Wang, C., Yang, H., Li, L., Deryng, D., Folberth, C., Liu, W., Makowski, D., Olin, S., Pugh, T.A.M., Reddy, A., Schmid, E., Jeong, S., Zhou, F., Piao, S., 2021. Global irrigation contribution to wheat and maize yield. Nat. Commun. 12 https://doi.org/10.1038/s41467-021-21498-5.

Xue, Q., Zhu, Z., Musick, J.T., Stewart, B.A., Dusek, D.A., 2006. Physiological mechanisms contributing to the increased water-use efficiency in winter wheat under deficit irrigation. J. Plant Physiol. 163, 154–164. https://doi.org/10.1016/j.jplph.2005.04.026.

Yang, M., Hassan, M.A., Xu, K., Zheng, C., Rasheed, A., Zhang, Y., Jin, X., Xia, X., Xiao, Y., He, Z., 2020. Assessment of water and nitrogen use efficiencies through

UAV based multispectral phenotyping in winter wheat. Front Plant Sci. 11 https://doi.org/10.3389/fpls.2020.00927.

Zhang, X., Zhang, X., Liu, X., Shao, L., Sun, H., Chen, S., 2015. Incorporating root distribution factor to evaluate soil water status for winter wheat. Agric. Water Manag. 153, 32–41. https://doi.org/10.1016/j.agwat.2015.02.001.

Zhou, Y., Lao, C., Yang, Y., Zhang, Z., Chen, H., Chen, Y., Chen, J., Ning, J., Yang, N., 2021. Diagnosis of winter-wheat water stress based on UAV-borne multispectral image texture and vegetation indices. Agric. Water Manag. 256, 107076 https://doi.org/10.1016/j.agwat.2021.107076.

Zia, S., Wenyong, D., Spreer, W., Spohrer, K., Xiongkui, H., Müller, J., 2012. Assessing crop water stress of winter wheat by thermography under different irrigation regimes in North China Plain. Int. J. Agric. Biol. Eng. 5, 24–34. https://doi.org/10.3965/j.ijabe.20120503.003.